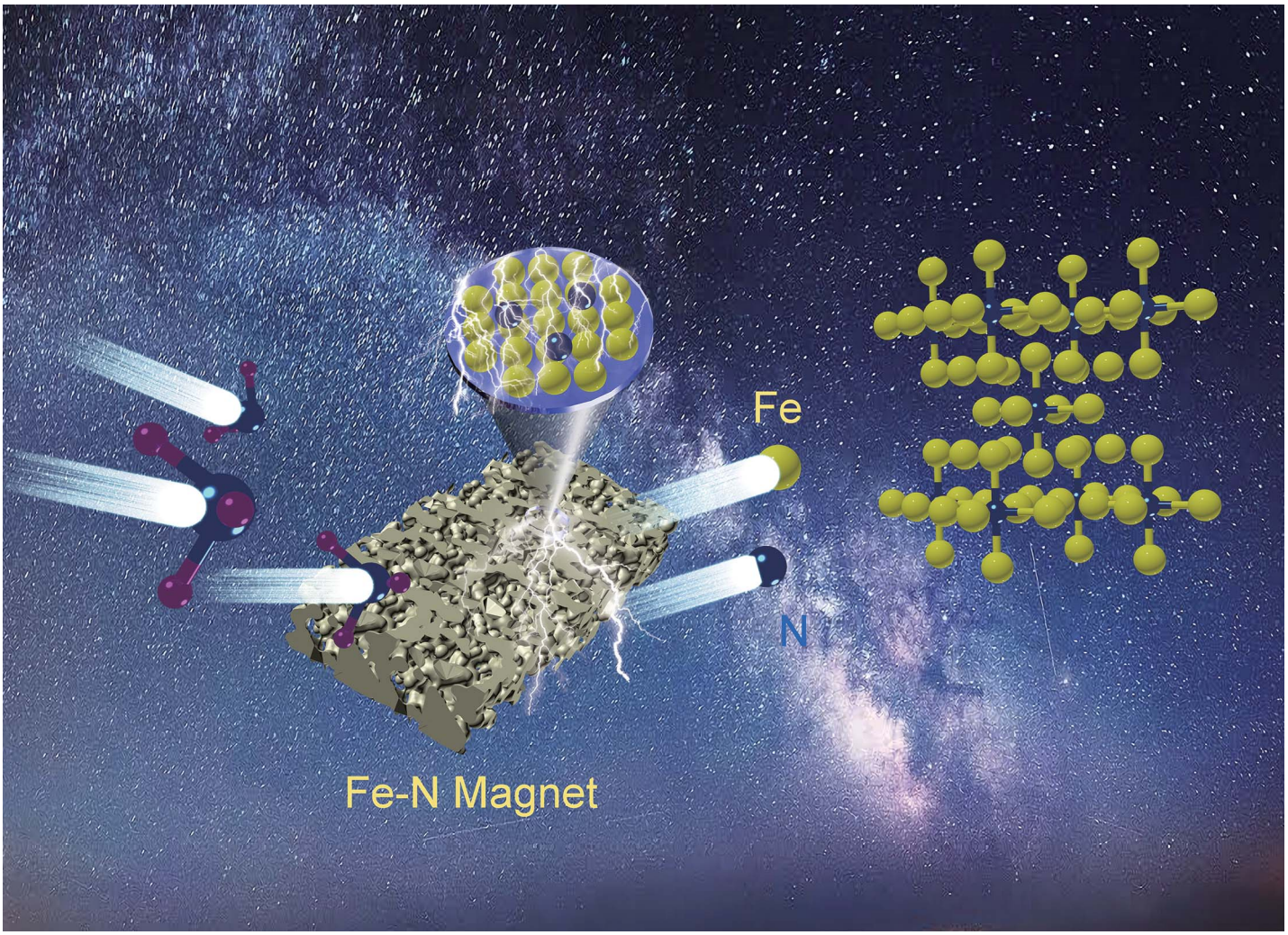

Showcasing research from Professor Jian-Ping Wang's laboratory, Department of Electrical and Computer Engineering, University of Minnesota, Minneapolis, United States.

Synthesis of α''-$Fe_{16}N_2$ ribbons with a porous structure

Formation of porous nanostructured ribbons was demonstrated in this work. The microstructure of Fe-based nanocomposite ribbons was modified to fabricate α''-$Fe_{16}N_2$ at 160 °C. The ribbons were heat treated first at 930 °C with an oxidation process, followed by a hydrogen reduction process at 350 °C. The reduced ribbons showed a porous nanostructure, which improved the nitrogen diffusion efficiency. This technique helped obtain the α''-$Fe_{16}N_2$ phase with a high volume ratio and a reasonably high coercivity. This technique could address potential challenges for a bottom-up approach to synthesize rare-earth-free α''-$Fe_{16}N_2$ magnets.

As featured in:

See Jian-Ping Wang *et al.*, *Nanoscale Adv.*, 2019, **1**, 1337.

ROYAL SOCIETY OF CHEMISTRY | Celebrating IYPT 2019

rsc.li/nanoscale-advances

Registered charity number: 207890

Nanoscale Advances

PAPER

View Article Online
View Journal | View Issue

Cite this: *Nanoscale Adv.*, 2019, **1**, 1337

Synthesis of α″-$Fe_{16}N_2$ ribbons with a porous structure†

Jinming Liu,[a] Guannan Guo,[a] Fan Zhang,[ab] Yiming Wu,[b] Bin Ma[a] and Jian-Ping Wang*[ab]

Received 4th January 2019
Accepted 3rd March 2019

DOI: 10.1039/c9na00008a

rsc.li/nanoscale-advances

The microstructure of FeCuB ribbons (~20 μm thick) was modified to fabricate α″-$Fe_{16}N_2$ at a temperature as low as 160 °C. The ribbon samples were heat treated first at a temperature reaching 930 °C and then quenched down to room temperature. During the heat treatment, ribbon samples were oxidized, and hydrogen reduction was then conducted to remove the oxygen from the ribbon samples. The reduced ribbon samples had a porous structure, which improved the nitrogen diffusion efficiency and decreased the fabrication temperature of α″-$Fe_{16}N_2$ down to 160 °C. It was demonstrated that the techniques for microstructure control in this method including oxidation and reduction helped obtain the α″-$Fe_{16}N_2$ phase with high coercivity, thus manifesting this could be a promising technique for low-temperature nitridation on ribbons in general.

Introduction

Permanent magnets (PMs) are widely used in the clean and renewable energy industry such as in electric motors[1] and wind turbines.[2] Rare-earth PMs such as Nd–Fe–B and $SmCo_5$ are in high demand since they have a high maximum energy product and a large magnetocrystalline anisotropy.[3] However, due to the concerns on the environmental degradation from mining rare-earth elements and cost issues,[4] research on rare-earth-free PMs has been attracting much more attention.[5,6] Magnetic materials with high saturation magnetization (M_s) and large magnetocrystalline anisotropy are good candidates. α″-$Fe_{16}N_2$ has been reported as a ferromagnetic material with a high M_s (~2.9 T).[7] After 40 years of debate, the existence and the physical origin of the giant saturation magnetization in $Fe_{16}N_2$ were finally confirmed.[8] It also possesses a large magnetocrystalline anisotropy (>1.0 × 10^7 erg cm^{-3}).[8–10] More importantly, both Fe and N are abundant and much cheaper than rare-earth elements. There were several successful efforts to synthesize α″-$Fe_{16}N_2$ nanoparticles (NPs) and powders in the past.[11–15] Recently, α″-$Fe_{16}N_2$ in bulk form with relatively high coercivity (H_c) were also reported.[15,16] All these properties make α″-$Fe_{16}N_2$ a promising candidate for rare-earth-free PMs.[17]

The α″-$Fe_{16}N_2$ phase was first reported by Jack in 1951.[18] In his method, nitridation was performed at a high temperature (>600 °C) using a gas mixture of ammonia and hydrogen since γ-FeN only exists at a temperature above 592 °C, based on the Fe–N binary phase diagram.[19] α′-Fe_8N was then formed by quenching γ-FeN to the martensite starting temperature and then α″-$Fe_{16}N_2$ could be obtained from α′-Fe_8N after a low-temperature (<200 °C) tempering process. The formation of the martensite Fe_8N phase was also reported by quenching the Fe-based nanocrystalline ribbons with γ′-Fe_4N phase.[20] However, the efficiencies of the α′-Fe_8N and α″-$Fe_{16}N_2$ phase transformations need to be further improved using these high-temperature nitridation processes.[21,22] In the late 1990s, a low-temperature nitridation (<200 °C) method was proposed to fabricate α″-$Fe_{16}N_2$ using α-Fe or iron oxide NPs as raw materials.[23,24] In the following decades, many research groups reported similar results.[13,25,26] Core–shell structured α″-$Fe_{16}N_2$ NPs were also synthesized using the low-temperature nitridation method, where the oxide shells were used to magnetically isolate α″-$Fe_{16}N_2$ NPs and enhance the H_c.[11,27] Up to now, only NPs, however, are used for the low-temperature nitridation method since they have a much higher surface to volume ratio that provides a higher nitridation efficiency. There are no reports on using several tens of micrometer thick ribbons as the starting material for the low-temperature nitridation method.

There were many reports on the successful attempts to lower down the nitridation temperature. Tong *et al.* experimentally demonstrated that the nitridation temperature of iron with the modified nanostructured surface layer could be as low as 300 °C, which is much lower than the conventional nitridation temperature.[28] In their experiment, surface mechanical attrition treatment was developed to generate a plastic deformation on the top surface layer of the bulk iron and a large number of grain boundaries were introduced, which enhanced the kinetics of nitridation at such a low temperature (300 °C). Grain

[a]*Department of Electrical and Computer Engineering, University of Minnesota, 200 Union Street SE, Minneapolis, MN, 55455, USA. E-mail: jpwang@umn.edu*

[b]*Niron Magnetics, 650 Taft St NE #400, Minneapolis, MN, 55413, USA*

† Electronic supplementary information (ESI) available. See DOI: 10.1039/c9na00008a

boundaries could also be introduced in Fe ribbons *via* thermal treatment.[29] Based on the Fe–N binary phase diagram,[19] body-centered cubic (bcc) Fe will transform into the face-centered cubic (fcc) Fe at a temperature of around 910 °C and new grain boundaries could be generated due to the phase transformation happening around this temperature. The grain boundaries obtained from the thermal treatment would help in enhancing the nitridation efficiency drastically. The oxidation and reduction processes were proved to be an effective way to synthesize α''-$Fe_{16}N_2$ by the low-temperature nitridation method.[12]

In this study, the oxidation and hydrogen reduction processes were used to modify the microstructure of melt-spun FeCuB ribbon samples, which were then used for the following low-temperature nitridation process to synthesize the α''-$Fe_{16}N_2$ phase directly. Fig. S1 in the ESI† shows the process flow chart and the expected microstructure (schematic) of the ribbon samples prepared at each stage. Cu and B were added to the ribbon samples to control their initial microstructure. B was used to fine-tune the grain structure of the melt-spun ribbons.[20] Meanwhile, based on the temperature–time-transformation (TTT) curve of Cu precipitation,[30] Cu could precipitate during the quenching process and work as either pinning sites (in grains) or magnetic isolation sites (at grain boundaries).

During the heat treatment process in an ambient condition, the ribbon samples were oxidized. The oxidized ribbons were then reduced using pure hydrogen gas at a relatively low temperature between 300 and 350 °C. After the hydrogen reduction, ribbons are expected to form a foam-like porous structure, which helps nitrogen atoms to diffuse into the ribbon samples. The oxidation of iron-based ribbons and the subsequent reduction may also generate micro-channels in the ribbons, which further enhance the nitridation efficiency in the grains.

Experimental details

Fe ribbons with 3 wt% Cu and 2 wt% B were prepared by a melt spinning system. The thickness of the ribbon is around 20 μm. First, a box furnace was heated up to 930 °C. The ribbons were put into the box furnace for a few minutes (8–16 min) and then were quenched in room-temperature distilled water. During this quenching process, the phase is transformed from bcc-Fe to fcc-Fe[19] and then back to bcc-Fe (or partial martensite phase), which would introduce new grain boundaries into the ribbon samples. Second, hydrogen reduction of the samples was carried out in a tube furnace at 300–350 °C for 2 h with a hydrogen flow rate of 40 sccm. The hydrogen reduction step is critical for the following nitridation process, and it could create micro-channels to enhance the nitrogen atom diffusion.[12,31] After that, the nitridation process was carried out in the same furnace at 160 °C for 42–84 h with an ammonia flow rate of 40–80 sccm. The ammonia flow rate is used to modify the nitridation potential, which is defined as the partial pressure of ammonia over the partial pressure of hydrogen $pNH_3/pH_2^{3/2}$ in the tube furnace.[19]

The crystal structures, the microstructures and the magnetic properties of the prepared ribbon samples were further characterized. The crystalline structures of the ribbon samples were examined by X-ray diffraction (XRD, Bruker 2D Discover D8). The microstructure of the ribbon samples was characterized using field-emission electron microscopy (FE SEM, Hitachi S-5000) and high-resolution transmission electron microscopy (HRTEM, FEI Tecnai G2 F30). The composition of the samples was determined by wavelength-dispersive X-ray spectroscopy (WDS). The magnetic properties were measured using a physical property measurement system (PPMS) with a vibrating sample magnetometer (Quantum Design).

Results and discussions

A. Crystalline structure analysis

The crystalline structures of the ribbon samples were characterized by XRD. Fig. 1 shows the XRD patterns of the raw ribbon sample, the quenched ribbon sample from 930 °C, and the ribbon sample after 350 °C/2 h hydrogen reduction. The primary phase of the raw ribbon sample is bcc Fe and there are also some other small diffraction peaks of iron oxide and boron oxide. The diffraction peak at around 69° is from the single crystal silicon holder used for the XRD measurement. The raw ribbons were heat treated at 930 °C and then quenched in room-temperature distilled water. Since the heat treatment was carried out in the air, the ribbon samples were also oxidized. Therefore, a reduction process was carried out to remove the oxygen from the ribbon sample to make it ready for the subsequent nitridation experiment. After the hydrogen reduction, the main phase became bcc Fe again.

Fig. 2 shows the XRD patterns of the ribbon samples after the nitridation process. The nitridation temperature was 160 °C and the ammonia flow rate was 80 sccm for the studied samples (Fig. 2(a)–(c)). An over-nitrided Fe_3N phase was observed even

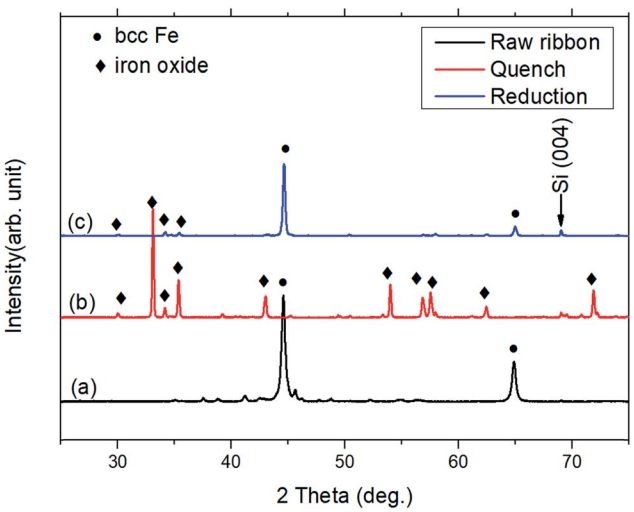

Fig. 1 XRD pattern of (a) raw ribbon sample; (b) ribbon sample after quenching from 930 °C in room temperature distilled water; (c) quenched ribbon sample after hydrogen reduction.

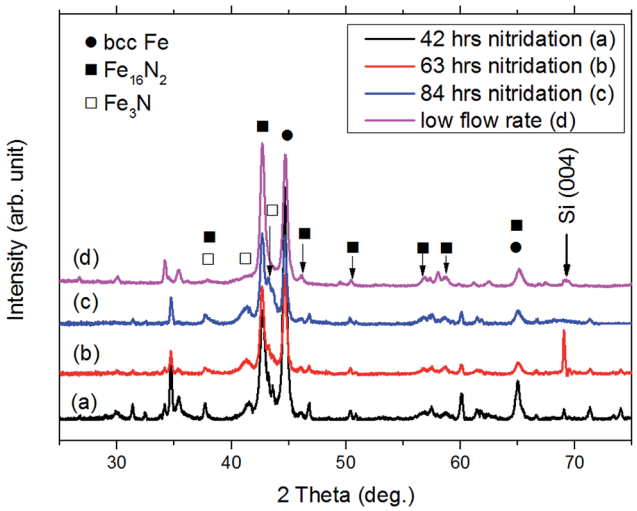

Fig. 2 XRD patterns of ribbon samples with different nitridation conditions: (a) 160 °C with 80 sccm ammonia for 42 h; (b) 160 °C with 80 sccm ammonia for 63 h; (c) 160 °C with 80 sccm ammonia for 84 h; (d) 160 °C with 40 sccm ammonia for 63 h.

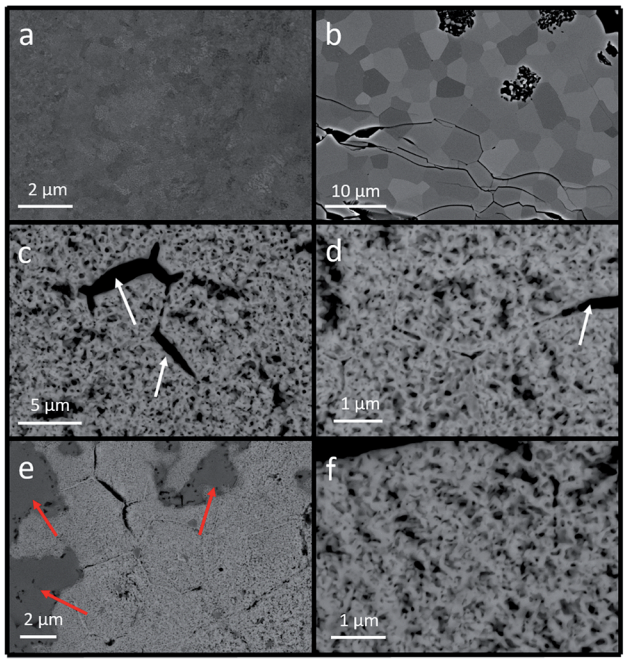

Fig. 3 SEM images of the ribbons: (a) raw ribbon sample, (b) ribbon sample quenched from 930 °C; (c) and (d) hydrogen-reduced sample at 350 °C with 40 sccm hydrogen for 2 h; (e) and (f) nitridation sample at 160 °C.

for samples with shorter nitridation time as 42 h. The high ammonia flow rate may provide very high nitridation potential for the ribbon producing the over-nitrided phase. To overcome this issue, a lower ammonia flow rate of 40 sccm was applied. The over-nitrided phase decreased drastically as shown in Fig. 2(d). Thus, the over-nitrided phase could be avoided by adjusting the nitridation potential. The X-ray diffraction patterns were also consistent with the published data where the α″-$Fe_{16}N_2$ phases and the over-nitrided phases using the low-temperature nitridation method were reported.[13,27] The over-nitrided phases were also reported in nanoparticle samples prepared by a low-temperature nitridation when the nitridation time was long (>42 h) and the nitridation temperature was relatively high (473 K).[13] Other diffraction peaks in the patterns of nitrided ribbon samples were from iron oxide, boron oxide, or iron boron oxide, which could also be disclosed by the element mapping as shown in Fig. 4 below.

B. Microstructure study of the ribbon samples

The microstructure of the ribbon samples is shown in Fig. 3. Fig. 3(a) is the SEM image of the raw ribbon sample. The raw ribbon sample was prepared by a melt-spinning system and the ribbon sample was quickly cooled and fine grains were observed compared with the oxidized ribbon sample. Fig. 3(b) is the SEM image of a quenched ribbon sample. During the heat treatment at 930 °C in an ambient condition, the grain boundary regions are oxidized; thus the grain structures can be clearly observed. Hydrogen reduction was conducted on the quenched sample to reduce iron oxides. Porous structures were obtained in the original grains as shown in Fig. 3(c) and (d). There were some black regions (marked with white arrows) in the hydrogen-reduced and nitrided ribbon sample, which could be due to the cracks inherited from the quenching step. The porous structures helped enhance the nitridation efficiency and more $Fe_{16}N_2$ phase could be obtained after the low-temperature nitridation.[12] The low-temperature nitridation experiment was carried out on the ribbon samples after hydrogen reduction in the same furnace and the SEM images of the nitridation samples are shown in Fig. 3(e) and (f). The microstructure of the nitrided sample is similar to that of the reduced sample since the nitridation was carried out at a temperature as low as 160 °C. The dark grey areas (marked with red arrows) in Fig. 3(e) and (f) are due to the oxidation of the sample.

In order to further investigate the microstructure of the nitrided samples, a cross-sectional SEM (X-SEM) image with elemental mapping was acquired as shown in Fig. 4. The thickness of the nitrided ribbon sample increased from 20 μm (thickness of the raw ribbon sample) to more than 50 μm, which could be due to the inward and outward growth of iron oxide during the heat treatment.[32] There are four regions in the ribbon sample as labeled in the XSEM image in Fig. 4(a). The elemental analysis of each region on the white square area marked in Fig. 4(a) was characterized (Fig. 4(b)–(f)). Based on the elemental mapping figures, most of the iron was located at the surface porous layer (region 4) and the center layer (region 1) as shown in Fig. 4(b). Iron in region 1 was also observed in the quenched ribbon sample (not shown here), indicating that the oxidation was not through the ribbon. Most of the nitrogen stayed at the porous layer (region 4) as shown in Fig. 4(c), demonstrating that the porous structure was preferred for nitrogen diffusion at 160 °C. In addition, it was difficult for nitrogen atoms to diffuse into regions 1–3. As shown in Fig. 4(d), most of the boron was located at regions 2 and 3 and much less boron migrated into the porous region 4. The

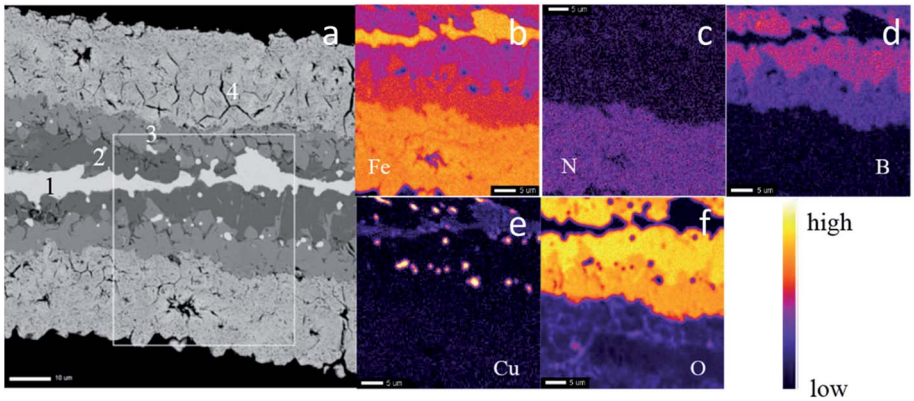

Fig. 4 XSEM and elemental mapping of a nitrided ribbon sample. The image to the left shows the cross-sectional SEM. The sample has a layered structure with five different elements analyzed, as labeled in image (a). The figures to the right are images of the different elements in the nitrided ribbon sample, Fe, N, B, Cu, and O.

distribution of copper in the ribbon sample is shown in Fig. 4(e). Some copper clusters were observed in regions 1–3 and there was a small amount of copper diffused into the porous region 4. The oxygen was mainly located in regions 2 and 3. By comparing the elemental mapping of iron, boron, and oxygen, we can conclude that there were iron boron oxides in regions 2 and 3. The oxides did not have the porous structure and few nitrogen atoms could diffuse into these regions. The existence of iron boron oxides in regions 2 and 3 is also consistent with the oxide diffraction peaks in the XRD patterns shown in Fig. 2.

TEM images were used to further characterize the microstructure and the $Fe_{16}N_2$ phase of the nitrided samples. The TEM images focused on the region with the porous structure (region 4 in Fig. 4). Fig. 5(a) and (b) show those porous structures that are consistent with the SEM images shown in Fig. 3 and 4. A high-resolution TEM (HRTEM) image was obtained as shown in Fig. 5(c) and the lattice fringes were observed. Indexing the crystal structure was done by obtaining the fast Fourier transform (FFT) of a grain marked by the red box in Fig. 5(c). The FFT patterns matched well with a $[1\bar{3}\bar{1}]$ zone axis diffraction pattern of α''-$Fe_{16}N_2$ structure as shown in Fig. 5(d).

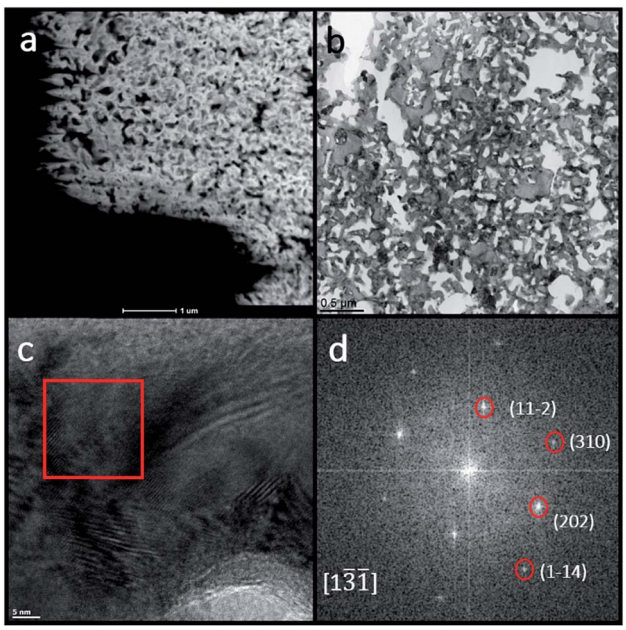

Fig. 5 TEM images of the porous region of a nitrided ribbon sample: (a) STEM image; (b) bright field image; (c) high resolution TEM image; (d) FFT patterns of the red box region in (c).

C. Magnetic properties

In-plane (IP) and out-of-plane (OP) hysteresis loops were measured by a VSM to characterize the magnetic properties of the ribbon samples prepared at different stages. IP loops were measured with the magnetic field parallel to the surface of the ribbon samples, while OP loops were measured with the magnetic field perpendicular to the surface. The definitions of IP and OP measurements are shown in Fig. 6(a). The hysteresis loops of the raw ribbon sample, quenched sample, and the reduced sample could be found in the ESI (Fig. S2†). The coercivity (H_c) of these samples is less than 100 Oe. The saturation magnetization (M_s) of the reduced ribbon sample is 160 emu g^{-1}, which is about 30 emu g^{-1} lower than that of the raw ribbon sample (~190 emu g^{-1}). This could be explained by the existence of a boron oxide layer in the reduced ribbon sample. Hysteresis loops of the nitrided sample are shown in Fig. 6(a). The in-plane coercivity (IP) H_c and the specific saturation magnetization (M_s) of the nitrided sample are 880 Oe and 145 emu g^{-1}, respectively. The lower M_s of the nitrided ribbon sample compared to that of the reduced ribbon sample might be due to the existence of some iron oxide phases in the region 4 as shown in Fig. 4 where iron nitride phases formed. The M_s and the H_c of the ribbon samples at each step are summarized in the ESI Fig. S3.† The M_s of the nitrided ribbon sample should be around 170 emu g^{-1} by subtracting the contribution of boron oxide since the weight ratio of N is ~3 wt% for $Fe_{16}N_2$ and the mass of the sample before and after nitridation is close. Based on the elemental mapping images shown in Fig. 4, the α''-$Fe_{16}N_2$ phase located at region 4 overlapped with the porous

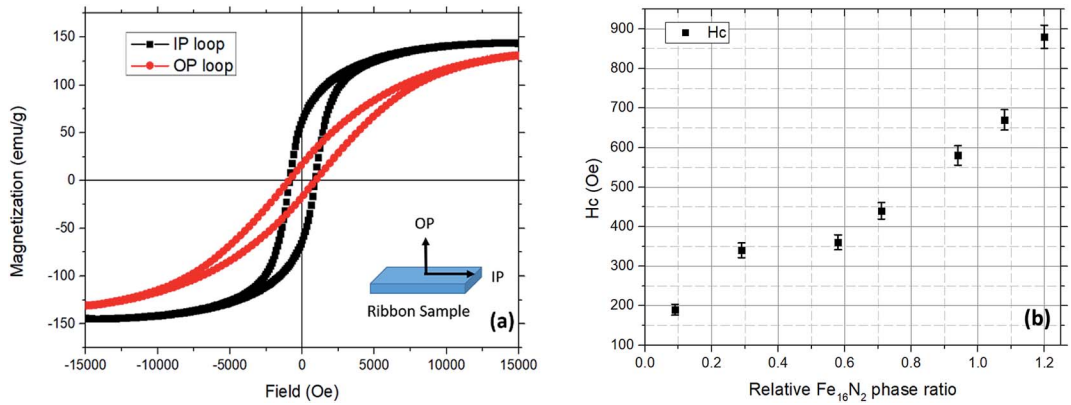

Fig. 6 (a) Typical hysteresis loops of the ribbon sample after nitridation. (b) Coercivity *versus* $Fe_{16}N_2$ phase ratio ($Fe_{16}N_2$ (202)/bcc Fe (110)).

structure. The relative low M_s of the nitrided sample is due to partial oxidation of the porous region as shown in Fig. 3(e) and (f). Ribbon samples with different nitriding parameters were prepared to investigate the relationship between the H_c and the relative phase ratio of α''-$Fe_{16}N_2$ as shown in Fig. 6(b). Herein, we define the relative phase ratio of α''-$Fe_{16}N_2$ as the intensity ratio of α''-$Fe_{16}N_2$ (202) over the sum of the intensities of α''-$Fe_{16}N_2$ (220) and bcc-Fe (110). It was found that H_c increased with the ratio of α''-$Fe_{16}N_2$, manifesting that the enhanced H_c was due to the hard-magnetic phase α''-$Fe_{16}N_2$.

The magnetic anisotropy constant of the nitrided sample was estimated using the law of approach to saturation.[33,34] The magnetization curve was measured using an applied magnetic field of up to 50 kOe. The effective magnetic anisotropy constant was estimated to be 3.6×10^6 erg cm^{-3}. Details of the calculations could be found in the ESI.† This effective anisotropy was smaller than that reported by other groups ($\sim 1.0 \times 10^7$ erg cm^{-3}).[25] Besides α''-$Fe_{16}N_2$, there were some other phases with relatively low magnetocrystalline anisotropy such as α-Fe and iron oxide in the nitrided ribbon sample as shown in both the XRD patterns and the XSEM elemental mappings. These phases are exchange coupled with the α''-$Fe_{16}N_2$ phase and the effective magnetic anisotropy of the whole sample was lower than what it should be.

Conclusions

α''-$Fe_{16}N_2$ phase was successfully obtained from melt-spun FeCuB ribbons by an integrated oxidation, reduction and nitridation process. The nitridation temperature of FeCuB ribbons after reduction was decreased to as low as 160 °C, which is much lower than that of the conventional case (>600 °C). The phase ratio of α''-$Fe_{16}N_2$ could be controlled by modifying the nitridation parameters. A small amount of Fe_3N phase was observed in the nitrided samples, which could also be reduced/eliminated by adjusting the nitridation potential. A porous structure was observed for the nitrided ribbon sample. The coercivity of the nitrided ribbon samples was found to be 880 Oe. It was also found that the coercivity increased with the increase in the volume of the α''-$Fe_{16}N_2$ phase. The relatively low coercivity could be attributed to the exchange coupling between the magnetic hard phase α''-$Fe_{16}N_2$ and other magnetic soft phases such as bcc Fe and iron oxide. Quenching and nitridation parameters could be further optimized to obtain pure α''-$Fe_{16}N_2$ phase.

Conflicts of interest

Dr Jian-Ping Wang has equity and royalty interests in and serves on the Board of Directors and the Scientific Advisory Board, for Niron Magnetics Inc., a company involved in the commercialization of FeN magnet. Jian-Ping Wang took an approved leave of absence from the University of Minnesota with a 70% appointment working at Niron from Feb 9th, 2018 to August 27th, 2018. The University of Minnesota also has equity and royalty interests in Niron Magnetics Inc. These interests have been reviewed and managed by the University of Minnesota in accordance with its Conflict of Interest policies.

Acknowledgements

Parts of this work were carried out in the Characterization Facility, University of Minnesota, which is partially supported by the National Science Foundation through the University of Minnesota MRSEC under Award Number DMR-1420013. Authors thank the partial support from the Institute for Rock Magnetism, Department of Earth Science, University of Minnesota, Twin Cities, for the use of instruments. We are grateful to Dr John Larson and Mr Chad Carda of Niron Magnetics Inc. for their help in ribbon preparation.

References

1 S. Chu and A. Majumdar, *Nature*, 2012, **488**, 294–303.
2 J. M. D. Coey, *J. Magn. Magn. Mater.*, 2002, **248**, 441–456.
3 S. Sugimoto, *J. Phys. D: Appl. Phys.*, 2011, **44**, 064001.
4 B. J. Smith and R. G. Eggert, *Environ. Sci. Technol.*, 2018, **52**, 3803–3811.
5 J.-R. Riba, C. López-Torres, L. Romeral and A. Garcia, *Renewable Sustainable Energy Rev.*, 2016, **57**, 367–379.

6 J. Cui, M. Kramer, L. Zhou, F. Liu, A. Gabay, G. Hadjipanayis, B. Balasubramanian and D. Sellmyer, *Acta Mater.*, 2018, **158**, 118–137.
7 Y. Sugita, H. Takahashi, M. Komuro, K. Mitsuoka and A. Sakuma, *J. Appl. Phys.*, 1994, **76**, 6637–6641.
8 J. P. Wang, N. Ji, X. Liu, Y. Xu, C. Sánchez-Hanke, Y. Wu, F. M. F. De Groot, L. F. Allard and E. Lara-Curzio, *IEEE Trans. Magn.*, 2012, **48**, 1710–1717.
9 H. Takahashi, M. Igarashi, A. Kaneko, H. Miyajima and Y. Sugita, *IEEE Trans. Magn.*, 1999, **35**, 2982–2984.
10 V. Zhukova, J. J. Val, M. Ilyn, M. Ipatov, R. Varga, C. Garcia and a. Zhukov, *J. Korean Phys. Soc.*, 2013, **62**, 1940–1944.
11 R. Zulhijah, A. B. Dani Nandiyanto, T. Ogi, T. Iwaki, K. Nakamura and K. Okuyama, *Nanoscale*, 2014, **6**, 6487.
12 R. Zulhijah, A. B. D. Nandiyanto, T. Ogi, T. Iwaki, K. Nakamura and K. Okuyama, *J. Magn. Magn. Mater.*, 2015, **381**, 89–98.
13 I. Dirba, C. A. Schwöbel, L. V. B. Diop, M. Duerrschnabel, L. Molina-Luna, K. Hofmann, P. Komissinskiy, H.-J. Kleebe and O. Gutfleisch, *Acta Mater.*, 2017, **123**, 214–222.
14 M. Q. Huang, W. E. Wallace, S. Simizu, a. T. Pedziwiatr, R. T. Obermyer and S. G. Sankar, *J. Appl. Phys.*, 1994, **75**, 6574.
15 Y. Jiang, M. Al Mehedi, E. Fu, Y. Wang, L. F. Allard and J. Wang, *Sci. Rep.*, 2016, **6**, 25436.
16 Y. Jiang, V. Dabade, L. F. Allard, E. Lara-Curzio, R. James and J.-P. Wang, *Phys. Rev. Appl.*, 2016, **6**, 024013.
17 J.-P. Wang, Y. Jiang, A. Mehedi and J. Liu, in *24th International Workshop on Rare-Earth and Future Permanent Magnets and Their Applications (REPM 2016)*, 2016, p. 1430.
18 K. H. Jack, *Proc. R. Soc. A*, 1951, **208**, 216–224.
19 E. H. D. M. van Voorthuysen, D. O. Boerma and N. C. Chechenin, *Metall. Mater. Trans. A*, 2002, **33**, 2593–2598.
20 M. Mehedi, Y. Jiang, B. Ma and J.-P. Wang, *Acta Mater.*, 2019, **167**, 80–88.
21 K. H. Jack, *J. Appl. Phys.*, 1994, **76**, 6620–6625.
22 M. Q. Huang, W. E. Wallace, S. Simizu, a. T. Pedziwiatr, R. T. Obermyer and S. G. Sankar, *J. Appl. Phys.*, 1994, **75**, 6574–6576.
23 A. Nagatomi, S. Kikkawa, T. Hinomura, S. Nasu and F. Kanamaru, *J. Jpn. Soc. Powder Powder Metall.*, 1999, **46**, 151–155.
24 T. Hattori, N. Kamiya and Y. Kato, *J. Magn. Soc. Jpn.*, 2001, **25**, 927–930.
25 T. Ogawa, Y. Ogata, R. Gallage, N. Kobayashi, N. Hayashi, Y. Kusano, S. Yamamoto, K. Kohara, M. Doi, M. Takano and M. Takahashi, *Appl. Phys. Express*, 2013, **6**, 073007.
26 K. Takagi, M. Akada, K. Ozaki, N. Kobayashi, T. Ogawa, Y. Ogata and M. Takahashi, *J. Appl. Phys.*, 2014, **115**, 103905.
27 T. Ogi, A. B. Dani Nandiyanto, Y. Kisakibaru, T. Iwaki, K. Nakamura and K. Okuyama, *J. Appl. Phys.*, 2013, **113**, 164301.
28 W. P. Tong, N. R. Tao, Z. B. Wang, J. Lu and K. Lu, *Science*, 2003, **299**, 686–688.
29 Z. Li, Q. Xu and B. Liu, *Comput. Mater. Sci.*, 2015, **107**, 122–133.
30 C. Zhang and M. Enomoto, *Acta Mater.*, 2006, **54**, 4183–4191.
31 L. Yu, C. Yang and Y. Hou, *Nanoscale*, 2014, **6**, 10638–10642.
32 V. B. Trindade, R. Borin, B. Z. Hanjari, S. Yang, U. Krupp and H.-J. Christ, *Mater. Res.*, 2005, **8**, 365–369.
33 J. P. Wang, D. H. Han, H. L. Luo, Q. X. Lu and Y. W. Sun, *Appl. Phys. A: Mater. Sci. Process.*, 1995, **61**, 407–413.
34 K. Ho, X. Xiong, J. Zhi and L. Cheng, *J. Appl. Phys.*, 1993, **74**, 6788–6790.